

Tilt and Azimuthal Angles of a Transmembrane Peptide: A Comparison between Molecular Dynamics Calculations and Solid-State NMR Data of Sarcolipin in Lipid Membranes

Lei Shi,[†] Alessandro Cembran,[†] Jiali Gao,[†] and Gianluigi Veglia^{†*}

[†]Department of Chemistry, and [‡]Department of Biochemistry, Molecular Biology, and Biophysics, University of Minnesota, Minneapolis, Minnesota

ABSTRACT We report molecular dynamics simulations in the explicit membrane environment of a small membrane-embedded protein, sarcolipin, which regulates the sarcoplasmic reticulum Ca-ATPase activity in both cardiac and skeletal muscle. In its monomeric form, we found that sarcolipin adopts a helical conformation, with a computed average tilt angle of $28 \pm 6^\circ$ and azimuthal angles of $66 \pm 22^\circ$, in reasonable accord with angles determined experimentally ($23 \pm 2^\circ$ and $50 \pm 4^\circ$, respectively) using solid-state NMR with separated-local-field experiments. The effects of time and spatial averaging on both ^{15}N chemical shift anisotropy and $^1\text{H}/^{15}\text{N}$ dipolar couplings have been analyzed using short-time averages of fast amide out-of-plane motions and following principal component dynamic trajectories. We found that it is possible to reproduce the regular oscillatory patterns observed for the anisotropic NMR parameters (i.e., PISA wheels) employing average amide vectors. This work highlights the role of molecular dynamics simulations as a tool for the analysis and interpretation of solid-state NMR data.

INTRODUCTION

Membrane proteins constitute ~15%–30% of all genomes (1) and play an important role in many processes such as signal transduction, ion conduction, and transport of small molecules and proteins. To date, the Protein Data Bank (PDB) contains <200 unique membrane protein structures, compared with >36,000 structures of soluble proteins (2). The disproportionately small number of membrane protein structures in the PDB is a result of several experimental challenges that hinder membrane protein structural characterization using x-ray crystallography and conventional solution-NMR techniques. These challenges include 1), poor recombinant expression systems; 2), difficulties in obtaining well-diffracting crystals for x-ray; and 3), the large size of protein/lipid complexes. Careful reconstitution of membrane proteins in detergent micelles often results in well-behaving samples suitable for solution-NMR analysis using TROSY-based techniques (3). Several outstanding examples have been reported in the literature and reviewed (4). Many detergents can interfere with membrane protein function, but there are examples where membrane proteins and enzymes are still functional under detergent solubilization, allowing for the characterization of protein native states and protein-protein interactions (5–8). However, detergent micelles represent only a rough approximation of membranes and fall short in reproducing characteristics of membrane bilayers such as lipid-water interface, fluidity, dynamics, and curvature.

Together with x-ray crystallography, solution NMR, and cryoelectron microscopy, solid-state NMR is becoming another high-resolution method for structure determination

of membrane proteins (9–14). This technique can be applied to membrane proteins reconstituted in lipid membranes, as the spectral resolution does not suffer as a result of the large size of membrane protein/lipid complexes. There are two major solid-state NMR approaches for determining the structure of membrane proteins: 1), magic-angle spinning NMR, using membrane proteins reconstituted in lipid vesicles; and 2), oriented solid-state NMR, using mechanically or magnetically oriented bilayer systems. Both methods can give site-specific resolution of protein resonances. Although the former can give high-resolution information also on the side-chain conformations, the latter has the advantage of simultaneously providing structure and topology of membrane proteins reconstituted in lipid bilayers (9,15).

For oriented solid-state NMR, membrane proteins are reconstituted either on mechanically aligned glass plates or in magnetically aligned bicelle samples. ^{15}N and ^{13}C labeled sites in the protein backbone are used as reporters of orientationally dependent chemical shift anisotropy (CSA) and dipolar couplings (DC). Recent successes in the application of these approaches include membrane active peptides (16), single-pass membrane proteins (17–20), membrane protein oligomers (21,22), and multispans membrane proteins (23,24). A similar approach has been pioneered by Killian and co-workers using orientationally dependent quadrupolar couplings measured on selectively ^2H -labeled Ala residues along the peptide sequence (the so-called GALA (geometric analysis of labeled alanines) method) (25), whereas Ulrich and co-workers utilize nonperturbing ^{19}F substitutions along peptides or protein side chains to obtain ^{19}F CSA (26,27).

A unifying element for all of these anisotropic properties is the wavelike patterns that they possess as a function of the residue number. These waves are two-dimensional

Submitted April 21, 2008, and accepted for publication February 12, 2009.

*Correspondence: vegli001@umn.edu

Editor: Mark Girvin.

© 2009 by the Biophysical Society
0006-3495/09/05/3648/15 \$2.00

doi: 10.1016/j.bpj.2009.02.025

projections of the protein's three-dimensional structure and orientation with respect to the lipid bilayers and can be converted into structural and topological restraints for structure determination (28–32).

As with all NMR parameters, these anisotropic chemical shifts and dipolar couplings are time-averaged properties and their values can be affected by protein internal dynamics. Although the dynamic effects are being analyzed and interpreted for residual CSA and DC measured in weakly aligned biomolecules (33–43), they have not been fully rationalized for membrane proteins in strongly aligned systems, with only a handful of studies carried out (44–46).

According to two recent studies (47,48), scaling of quadrupolar couplings due to side-chain dynamics results in underestimation of the tilt angle of helical membrane peptides embedded in lipid membranes. Specifically, after analyzing molecular dynamics (MD) trajectories, it was concluded that there was a 30° discrepancy between the calculated and the experimental tilt angles. Both groups suggested that ¹⁵N data obtained from separated-local-field experiments would give a more faithful estimation of both the tilt and azimuthal rotation angles of membrane proteins in lipid bilayers (47,48). A recent article by Koeppe and co-workers reconciles the experimental topology derived from both ¹⁵N CSA and DC with that of the GALA method (49), highlighting the precision of both approaches in determining the membrane protein topology. This contrasts with work carried out by Watts and co-workers (45,46), who found that fast structural fluctuations (rotation, librations, etc.) that occur in transmembrane peptides affect the appearance of the wavelike patterns (or polarization index slant angle (PISA) wheels) derived from the separated-local-field experiments, jeopardizing both the assignment and interpretation of experimental data and raising more questions regarding the role of the dynamics (45). To what extent do protein dynamics affect CSA, DC, and the wavelike pattern on aligned systems? Is this effect common to all proteins? Can MD calculations assist the resonance assignment process? To answer these questions, we have carried out molecular dynamics simulations on monomeric sarcolipin (SLN), which we have characterized extensively using both solution NMR in micelles and solid-state NMR in lipid bilayers (7,17,50–52). SLN is a 31-amino-acid, single-pass membrane protein that regulates the sarcoplasmic reticulum Ca²⁺-ATPase (SERCA) in both fast- and slow-twitch muscle fibers by lowering the apparent affinity of SERCA for Ca²⁺ in a manner similar to phospholamban (53,54). The structures determined by solution NMR data in sodium dodecyl sulfate and dodecylphosphocholine micelles (7,52) show that SLN comprises four different domains: a short unstructured N-terminus (residues 1–6), a short helical domain Ib (residues 7–15), a more dynamic helical domain II (residues 16–26) and the unstructured C-terminus (residues 27–31) (Fig. 1). Solid-state NMR polarization inversion spin exchange at magic angle (PISEMA) experiments (55) carried

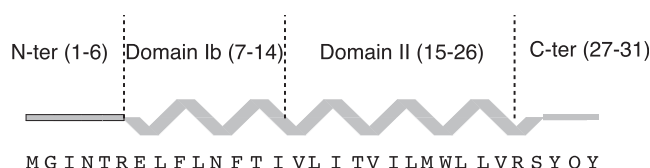


FIGURE 1 SLN primary sequence and definition of dynamic domains according to Buffy and co-workers (7).

out on selective labeled SLN reconstituted in mechanically aligned lipid bilayers show a well defined PISA wheel. Using a static model with an ideal helix to fit the experimental PISA wheel pattern, it was determined that monomeric SLN adopts a tilt angle of $\sim 23 \pm 2^\circ$ with respect to the membrane normal (17). Starting from the structure determined in detergent micelles, we carried out MD simulations of monomeric SLN in pure 1,2-dioleoyl-*sn*-glycero-3-phosphocholine (DOPC) lipid bilayers and compared the calculated topology with that derived from solid-state NMR experiments (PISA wheel). Specifically, we analyzed the time evolution of the tilt and azimuthal rotation angle of SLN during 150 ns of molecular dynamics simulations. The NMR parameters back-calculated from molecular dynamics trajectories are in agreement with those measured using solid-state NMR spectroscopy (separated-local-field experiments).

THEORY AND METHODS

Initial setup

The starting structure of SLN was selected from the conformational ensemble derived from a solution NMR study (PDB code: 1jdm) (52). The protein was treated as a rigid body and equilibrated into a hydrophobic slab of adjustable thickness. The initial orientation of SLN was obtained from the OPM (orientations of proteins in membrane) database (56). The depth of insertion of the transmembrane residues and the orientation of the protein were determined by minimizing the free energy of transfer from water to lipids (56). The initial tilt angle obtained with this method was $1 \pm 7^\circ$. Subsequently, SLN was embedded in an implicit membrane using the generalized Born model with simple switching function (GBSW) (57), where the anisotropic membrane environment was modeled by different dielectric constants. The bilayer hydrocarbon core was represented by a low dielectric region ($\epsilon = 2$, thickness ~ 30 Å). The bulk water region was approximated by $\epsilon = 80$ and the interface region (a 2.5-Å slab) had a dielectric constant between those of the water and the hydrocarbon core. This was accomplished by using a simple switching function. The total membrane thickness was set to 35 Å, a value experimentally determined for the L_α phase (58,59). Molecular dynamics simulations were performed for 2 ns at a temperature of 298 K. The resulting tilt angle of SLN was $17 \pm 6^\circ$. This configuration was saved for subsequent MD simulations in explicit DOPC lipid bilayers. The calculations with explicit bilayers were performed using the program CHARMM, Version 33a2 (60), utilizing the PARAM27 force field with the CMAP correction (61–63).

To build the DOPC bilayer, we used a protocol developed by Woolf and Roux (64,65). The lipid headgroups were initially represented by effective Lennard Jones spheres and were placed at $+17.5$ Å and -17.5 Å along the *z* direction (66,67) with respect to the center of the bilayer to mimic a membrane thickness of 35 Å. After energy minimization, the Lennard-Jones spheres were replaced by prehydrated DOPC molecules taken from the CHARMM library. Lipid rotation and translation were successively

applied during energy minimization steps to relax the system and to avoid close contacts. Then, two preequilibrated hexagonal water boxes were placed at the top and the bottom of the lipid membrane containing SLN to obtain the desired level of hydration of the lipids. Successive minimization using steepest-descent and Newton-Raphson methods was applied to minimize the initial configuration of the SLN/DOPC system. The cross-sectional area of one DOPC phospholipid was 74 \AA^2 . The entire bilayer system was constructed using 27 DOPC molecules for the top and the bottom layer, resulting in a total of 54 DOPC molecules in the xy (membrane) plane. Hexagonal periodic boundary conditions were used with a unit cell of $50 \text{ \AA} \times 50 \text{ \AA} \times 80 \text{ \AA}$. The final system consists of a total of 18,090 atoms, including 549 atoms from SLN, 7452 atoms from the 54 DOPC lipids, 10,080 atoms from 3360 waters using the three-point-charge TIP3P model (68) and counter anions, which were added to neutralize the system and achieve an ionic strength near physiological conditions. To gradually relax the protein, harmonic restraints on the backbone and side chains of SLN were added and then slowly removed during the initial energy minimization and the early equilibration period using Langevin molecular dynamics. The SHAKE algorithm was applied to constrain the distances of all covalent bonds involving hydrogen atoms (69). This allowed us to use an integration time step of 2 fs. To compute the nonbonded interactions, the van der Waals terms were evaluated using an atom-based cutoff scheme feathered to zero between 10 and 16 \AA with a switching function. The particle-mesh Ewald (PME) method was used for the Coulomb terms, avoiding truncation of the long-range electrostatic interactions (70–72). We used a charge mesh of $48 \times 48 \times 81$ grid points, at a spacing of $\sim 1 \text{ \AA}$, along with the Ewald parameter, $\kappa = 0.34 \text{ \AA}^{-1}$, and a direct interaction distance of 16 \AA . A constant temperature of 310 K was maintained using the Nosé-Hoover chain (73,74). Pressure was kept constant at 1 atm along the z direction by Langevin piston Nosé-Hoover (75,76) with the xy area fixed. To prevent translational drift of the protein, a cylindrical potential function was applied on SLN heavy atoms to remove the center-of-mass dynamics along the z axis for the first 4 ns. In addition, a planar potential function was applied on DOPC lipid headgroups to prevent the translational drift of the bilayer and at the same time keep the center of mass of lipids close to the xy plane. After 4 ns of MD simulation, all the constraints were removed and the system was further simulated up to a total of 150 ns. The first 10 ns were discarded and the last 140 ns were selected for the final analysis. The simulations and analyses were carried out on the SGI (Sunnyvale, CA) Altix Cluster at the Minnesota Supercomputing Institute.

Analysis of fast motion (picoseconds to nanoseconds)

The generalized order parameter S^2 was calculated using the long-time tail of the second-order Legendre function of the correlation function for each NH vector (\vec{v}) of the protein backbone,

$$S^2 = \lim_{t \rightarrow \infty} C_2(t),$$

where

$$C_2(t) = \langle P_2(\vec{v}(\tau) \cdot \vec{v}(\tau + t)) \rangle_\tau.$$

$P_2(x) = \frac{1}{2}(3x^2 - 1)$ is the second-order Legendre polynomial. The angular brackets represent the ensemble average over the MD trajectories. The unit vectors $\vec{v}(\tau)$ and $\vec{v}(\tau + t)$ describe the orientation of NH bond vectors at time τ and $\tau + t$ with respect to a fixed reference frame. The reference frame is constructed by removing the translational and rotational motion in the MD trajectory by least root-mean-square (RMS) fitting of the backbone atoms onto the starting structure, which was performed using the ANALYSIS module of the CHARMM package (60).

Experimental spin relaxation data (R_1 , R_2 , and heteronuclear nuclear Overhauser effects) were taken from our previous work on SLN reconstituted in dodecylphosphocholine micelles (7). The data were analyzed using the model-free approach, according to the Lipari-Szabo formalism (77). The simulations were carried out using MODELFREE software package interfaced with FastModelFree (78). Model selection was performed by the

fastModelFree software according to the method proposed by Mandel et al. (79). An axially symmetric diffusion model was able to fit the relaxation data for all of the protein amide sites. There was no difference between the order parameters obtained from the axially symmetric diffusion model and those from the isotropic overall diffusion model (data not shown).

Essential dynamics using principal component analysis

To extract the large amplitude motions of SLN during the MD simulations and project their effects on the PISEMA spectra, the molecular dynamics trajectories were analyzed using principal component analysis (PCA). PCA is a powerful method for extracting large-scale, low-frequency motions from MD trajectories (80,81). PCA is based on the diagonalization of a covariance matrix C , which contains the atomic fluctuation around the average atomic positions.

$$C_{ij} = \left\langle (r_i(t) - r_i^m)(r_j(t) - r_j^m) \right\rangle$$

Here, C_{ij} represents an element in covariance matrix C , r_i is the position for atom i , and r_i^m is the mean position. To focus on the intrinsic dynamics of protein SLN, translational and rotational motions are removed by superimposing each structure to the reference configuration by means of least-RMS deviation (RMSD) before analysis. We obtain a set of eigenvalues and the corresponding eigenvectors by diagonalizing C . The eigenvectors correspond to the quasi-harmonic motions of individual modes and the eigenvalues represent the mean square fluctuations along the eigenvectors. The eigenvalues are usually selected based on their amplitude and referred to as principal components (PCs). The first (lowest) eigenvalue corresponds to the largest fluctuation of the system along the first eigenvector. In fact, the overall dynamic fluctuations of the protein can be described by just a few “essential” eigenvalues with large amplitudes.

It is possible to project the structure on to an eigenvector using the relationship

$$q_l = (\vec{r} - \langle \vec{r} \rangle) \cdot \vec{\eta}_l,$$

where q_l is the displacement of the structure along the l th eigenvector with respect to the average structure, \vec{r} is the coordinate vector of a given structure, $\langle \vec{r} \rangle$ is the vector of the average structure, and $\vec{\eta}_l$ is the eigenvector. The 3-D structure corresponding to a displacement along a single eigenvector can be calculated using

$$\vec{r} = q_l \vec{\eta}_l + \langle \vec{r} \rangle.$$

This provides a way to visualize the quasi-harmonic motions of a specific mode, represented by the average structure. For PCA analysis of SLN, we used the software Bio3d, which was developed for comparative analysis of protein structures (82).

Back calculations of PISEMA spectra from MD trajectories

The formalism developed by Cross and co-workers was used to calculate PISEMA spectra (83). In PISEMA experiments, both chemical shift anisotropy (CSA) and dipolar coupling (DC) tensors are measured at a fixed orientation with respect to the direction of the static magnetic field \vec{B}_0 . The CSA tensor is asymmetric and its principal axis frame (PAF) can be described in terms of its principal components $\vec{\sigma}_{11}, \vec{\sigma}_{22}, \vec{\sigma}_{33}$ as follows:

$$\text{PAF} = (\vec{\sigma}_{11}, \vec{\sigma}_{22}, \vec{\sigma}_{33}),$$

where diagonal elements are arranged such that $\sigma_{33} > \sigma_{22} > \sigma_{11}$. The scalar value of the CSA tensor can be rewritten as a function of its principal components as

$$\sigma = \sigma_{11}(\vec{B}_0 \cdot \vec{\sigma}_{11})^2 + \sigma_{22}(\vec{B}_0 \cdot \vec{\sigma}_{22})^2 + \sigma_{33}(\vec{B}_0 \cdot \vec{\sigma}_{33})^2.$$

The DC tensor ν is traceless and axially symmetric, with a unique rotation axis (\vec{u}) around the covalent NH bond, and can be expressed as

$$\nu = \frac{\nu_{\parallel}}{2}(3(\vec{B}_0 \cdot \vec{u})^2 - 1),$$

where ν_{\parallel} is the value of the DC tensor when $\vec{B}_0 = \vec{u}$, i.e., it occurs when the NH bond vector is in line with the direction of the magnetic field. In the MD trajectory, \vec{B}_0 is set to a unit vector along the z axis that is parallel to the membrane normal. If (x, y, z) are the coordinates for the unit vector \vec{B}_0 in the PAF, then DC and CSA can be expressed as:

$$\sigma = \sigma_{11}x^2 + \sigma_{22}y^2 + \sigma_{33}z^2$$

$$\nu = \frac{\nu_{\parallel}}{2}[3(\cos \alpha \sin \beta \cdot x + \sin \alpha \sin \beta \cdot y + \cos \beta \cdot z)^2 - 1],$$

where \vec{u} is the direction of the unit NH bond vector, α is the polar angle made by \vec{u} and the peptide plane, and β is the polar angle between \vec{u} and σ_{33} . In the above equations, we have the relationships $x^2 + y^2 + z^2 = 1$ and $\nu_{\parallel} = A\gamma_1\gamma_2/r^3$, where γ_1 and γ_2 are the gyromagnetic ratios of nuclei 1 and 2, r is the distance between the two atoms, and A is a constant equal to $\mu_0 h/2\pi$, with μ_0 being the vacuum permeability and h being Planck's constant. Assuming a planar peptide structure, we have $\alpha = 0^\circ$ and $\beta = 17^\circ$, which is determined experimentally (84). The principal components of the CSA tensor are obtained from the experimental PISEMA powder pattern and assumed to be the same for all residues ($\sigma_{11} = 57.3$ ppm, $\sigma_{22} = 81.2$ ppm, $\sigma_{33} = 228$ ppm) (10). The coefficient for the DC is 10.74 kHz, with the NH bond distance equal to 1.042 Å (10). These numerical values are nontrivial approximations employed to simplify the calculations (different residues usually have different values of CSA tensors). The NH bond length used in CHARMM force field is 0.99 Å (60).

RESULTS

Interactions between SLN and its environment

Molecular dynamics simulations of SLN embedded in DOPC bilayer in water were performed for a total of 150 ns. Fig. 2 A shows the density profile of the lipid bilayer principal structural groups along the z direction after the initial 4 ns of MD calculations. The time-average distribution profile for DOPC bilayer in the presence of SLN corresponds to a typical liquid crystalline ($L\alpha$) phase (85). Under these conditions, the lipid bilayer is divided into interfacial and hydrocarbon regions, with the hydrocarbon center populated by methyl, methylene, and unsaturated groups of the oleoyl moieties. The interfacial region, on the other hand, is dominated by the presence of glycerol, phosphate, and choline groups, with the water molecule profile intercalating into the bilayer core up to the unsaturated carbon of the oleoyl moieties (85).

Based on analysis of the primary sequence, SLN displays the characteristic properties of transmembrane proteins, including a cluster of hydrophobic residues, charged amino acids flanking the transmembrane domain, and an aromatic belt that anchors the protein to the bilayer. To analyze the distributions of these residues during the MD simulations, the amino acids were classified as hydrophobic and hydro-

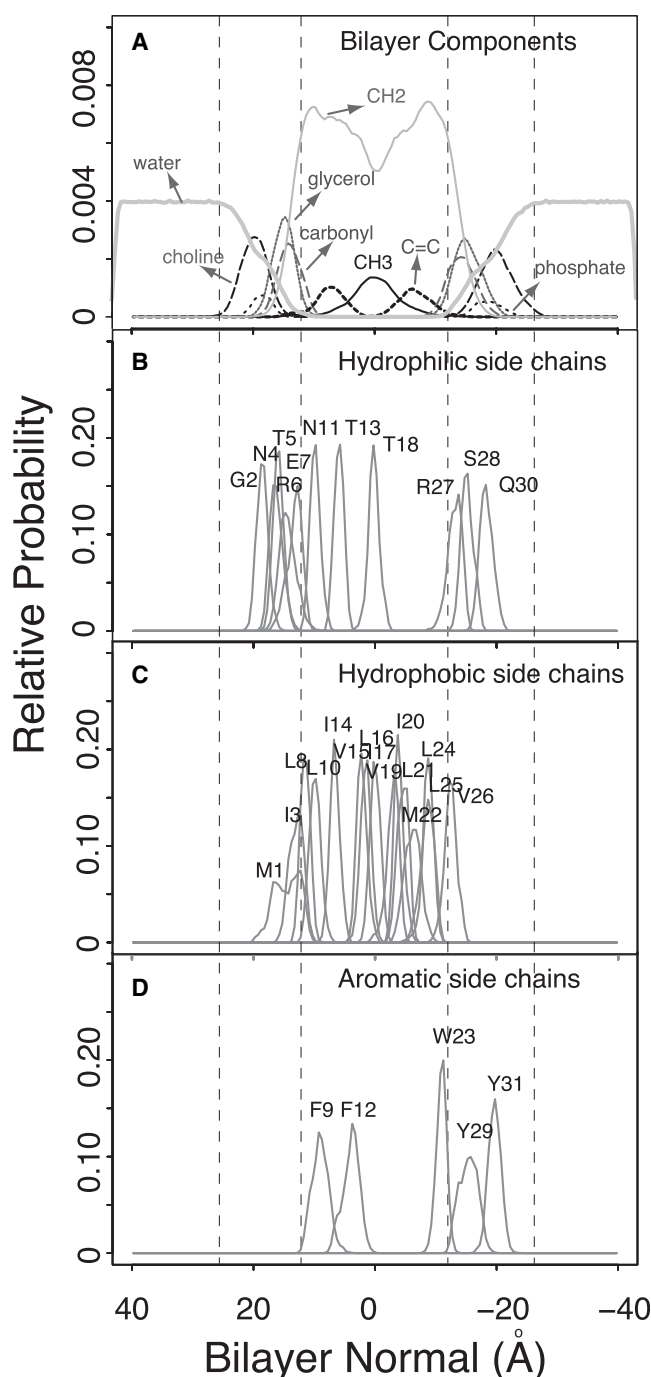


FIGURE 2 (A) Atomic density profiles of the bilayer components along the bilayer normal. (B–D) Distribution of the centers of mass of the hydrophilic (B), hydrophobic (C), and aromatic (D) side chains of SLN amino acids. The partition between hydrophilic and hydrophobic was carried out according to the hydrophobicity scale by White and co-workers (86).

philic based on the hydrophobicity profile by Wimley and White (86).

The distributions of the amino acids within the DOPC bilayer are reported in Fig. 2, B–D. As expected, the hydrophobic amino acids populate the inner core of the membrane bilayer, whereas the charged residues located at both termini

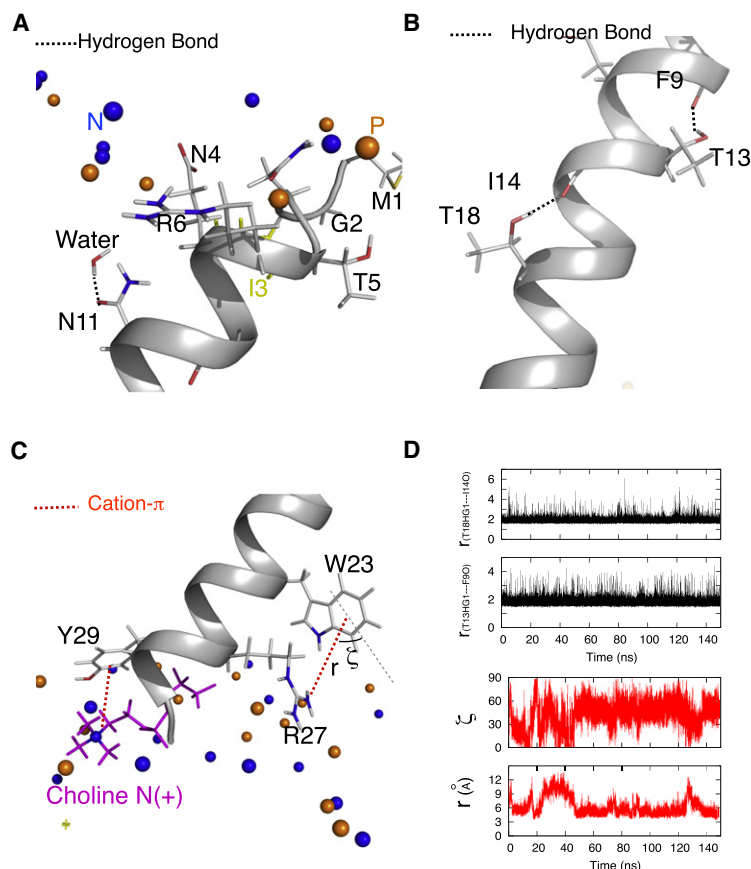


FIGURE 3 (A) Snapshot (95 ns) of the SLN N-terminal portion showing the interactions between N11 with water molecules. The I3 sidechain points toward the hydrophobic core. (B) Snapshot of domain Ib showing the hydrogen bonds formed by T13 and T18 with the SLN backbone carbonyls of F9 and I14. (C) Snapshot of the C-terminal domain with cation- π interactions between R27 and W23, and of the choline group with Y29. (D) Plots of the distance versus time between γ protons of the T13 and T18 side chains and F9 and I14 carbonyl groups (upper panels), and of distance r between the R27 side-chain N and the center of mass of the W23 aromatic ring, and the angle ζ between r and the aromatic ring.

populate the water/headgroup interfaces. R6 and R27 are distributed around the interfacial region, forming salt bridges with the lipid headgroups. T5 (the putative phosphorylation site of SLN (87)) forms hydrogen bonds with a lipid headgroup near the glycerol/choline group interface. N11 leans toward the lipid headgroups, making a hydrogen bond with a water molecule (Fig. 3 A). It is interesting that T13 and T18 are distributed in the center of the hydrocarbon region of the lipid bilayer and their polar hydroxyl groups form hydrogen bonds with the backbone carbonyl groups of F9 and I14, respectively (Fig. 3 B). The propensity of threonine residues to form hydrogen bonds with the protein backbone has been pointed out already by Johansson and Lindahl (88). The aromatic side chains of F9 and F12 located toward the N-terminus intercalate in the lipid apolar region, keeping the average orientation of the aromatic rings parallel with respect to the lipid chains. This configuration is common for phenylalanine residues of membrane-embedded polypeptides and maximizes their packing efficiency within the lipid membranes (88–90). The tryptophan side chain is located in the other leaflet of the membrane bilayer, with its polar indole group directed toward the interfacial region (Fig. 3 C), though it did not form any interactions with the polar headgroups throughout the simulations. It is interesting that R27 and W23 seem to be stabilized by cation- π interactions. This is indicated by the close distances of the arginine

side chain and the centroid of the tryptophan ring (Fig. 3 D). To calculate these distances, we utilized the convention described by Nielsen and co-workers (91). Y29 can also form cation- π interactions with the positively charged nitrogen atom in the choline group (Fig. 3 C), anchoring the C-terminus of SLN to the lipid bilayer. Note that these aromatic residues are believed to be necessary for membrane localization of SLN in the sarcoplasmic reticulum and for interaction with SERCA (92).

Structural dynamics and topology of SLN in lipid bilayers

According to NMR analysis in detergent micelles, SLN can be partitioned into four dynamic domains: two mobile termini (N-terminus, 1–6, and C-terminus, 27–31), a short dynamic helix domain Ib (residues 7–14), and a more rigid helix domain II (residues 15–26) (7). The structural changes of SLN throughout the MD simulation were analyzed by examining the histogram of the RMSDs of each domain as functions of time (Fig. 4 A). It is apparent that the system has reached a stable conformation for an extended period of time during MD simulations. After 10 ns, the SLN backbone showed RMSD values fluctuating ~ 1.6 Å, indicating significant structural changes. This is primarily due to the flexible N-terminus that undergoes significant migrations

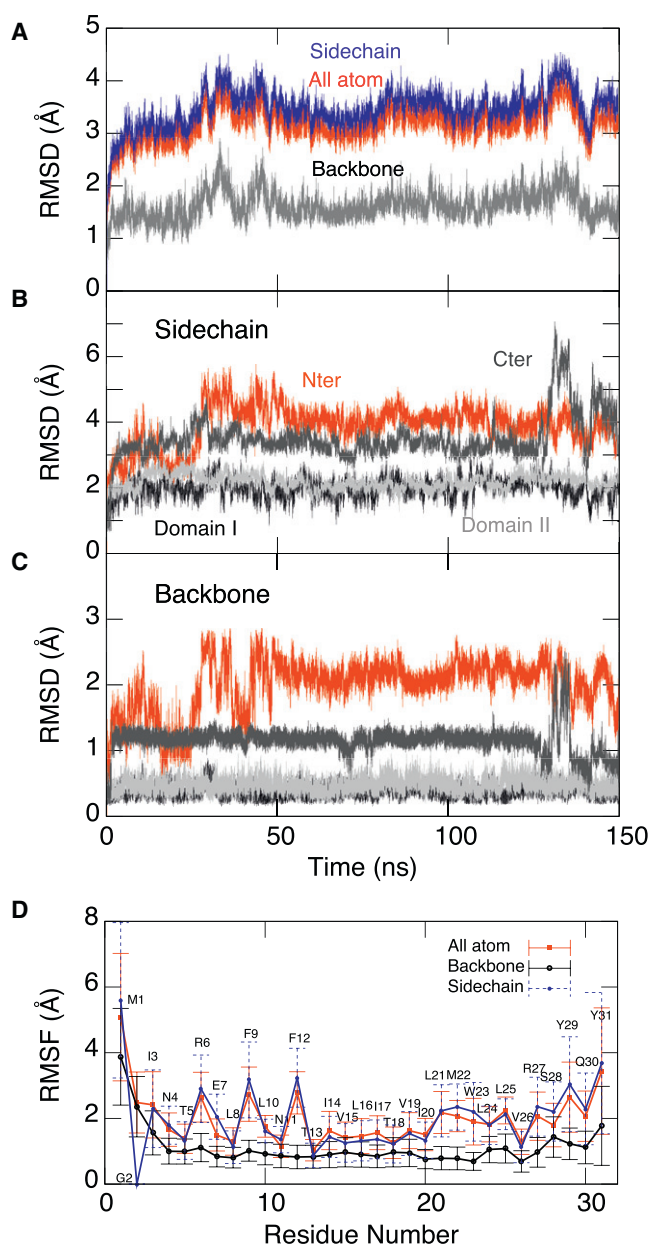


FIGURE 4 (A) Histograms of the RMSD with respect to time for the SLN backbone, side chain, and all-atom domains during the MD simulations. (B) Contribution of the SLN N-terminus, domain Ib, domain II, and the C-terminus to the RMSD of the side chain. (C) Contribution of the SLN N-terminus, domain Ib, domain II, and the C-terminus to the RMSD of the backbone. (D) RMSFs of all atoms, backbone atoms, and side-chain atoms during the MD simulations.

near the lipid headgroups and converges to a set of stable configurations. In contrast, the two helical domains, Ib and II, and the C-terminal portion of the protein are stable throughout the simulations, with domain Ib slightly more flexible than domain II. This is consistent with both relaxation data and solvent-accessibility measurements carried out using solution NMR in DPC micelles (7). The time-averaged RMS fluctuations (RMSF) for each residue give a more

complete picture of the local protein flexibility (Fig. 4 D). Overall, the RMSF values of the side chains are greater than those for the backbone atoms, indicating higher flexibility. The side chains for both termini are more flexible than those in the central portion of SLN, comprising residues 13–20. It is of interest that the side chains for residues in domain Ib show periodic oscillation, with R6, F9, and F12 displaying greater mobility. In general, it is expected that longer side chains would display higher RMSF values than shorter side chains (Ala, Gly). However, residues E7, L8, L10, and N11, which possess long side chains, show substantially lower RMSF values relative to those of R6, F9, and F12. Since these residues are positioned in the same face of the domain Ib helix, it is possible that one face of the helix is more dynamic than the other.

To analyze the topology during MD trajectories, the helical domain of SLN was first considered as a continuous helix and the topology was analyzed by reporting the azimuthal angle, ρ , and the overall tilt angle, θ . The SLN helical axis was defined using the convention described by Aqvist and co-workers (93). The overall SLN tilt and azimuthal angles are reported in Fig. 5. As mentioned in the Methods section, the molecular dynamics carried out in the implicit solvent resulted in an overall tilt angle of $17 \pm 6^\circ$. After an abrupt initial excursion (during the first 5 ns), the SLN tilt angle oscillates around $28 \pm 6^\circ$. The calculated tilt is in good agreement with the experimental data, derived from PISEMA experiments. In fact, from the structural fitting of the experimental PISA wheel with a static ideal helix model, it was found that θ is $23 \pm 2^\circ$. Note that the MD simulations were carried out in pure DOPC, whereas the solid-state NMR experiments were performed with a mixture of DOPC/DOPE. It has been reported that the closer packing of the PE causes an increase of bilayer thickness that in turn would cause SLN to tilt $<25^\circ$ (94). In agreement with previous studies (25,95,96), this could cause an increase in the computed tilt angle of SLN. Although the MD simulations described here were performed for 150 ns, this is still short with respect to the timescales probed by the PISEMA experiments. Improved statistical results may be obtained by running multiple 150-ns simulations or by significantly extending the overall computational time. Finally, the experimental tilt angle was determined using a limited number of amide sites and an ideal helix to fit the overall spectral pattern (17).

A parameter important for defining the topology within lipid bilayers is the azimuthal (or rotation, ρ) angle of SLN around its helical axis. The azimuthal angle of a helical protein in lipid bilayers is an index of the specific interactions occurring between the protein side chains and the lipid membranes that can be obtained from the PISA wheel derived from PISEMA experiments (81,97). To calculate ρ , we choose the starting configuration of SLN as a reference frame and use a method similar to that of Killian and Delgado (47,48), as depicted in Fig. 5 A. Fig. 5 A shows the

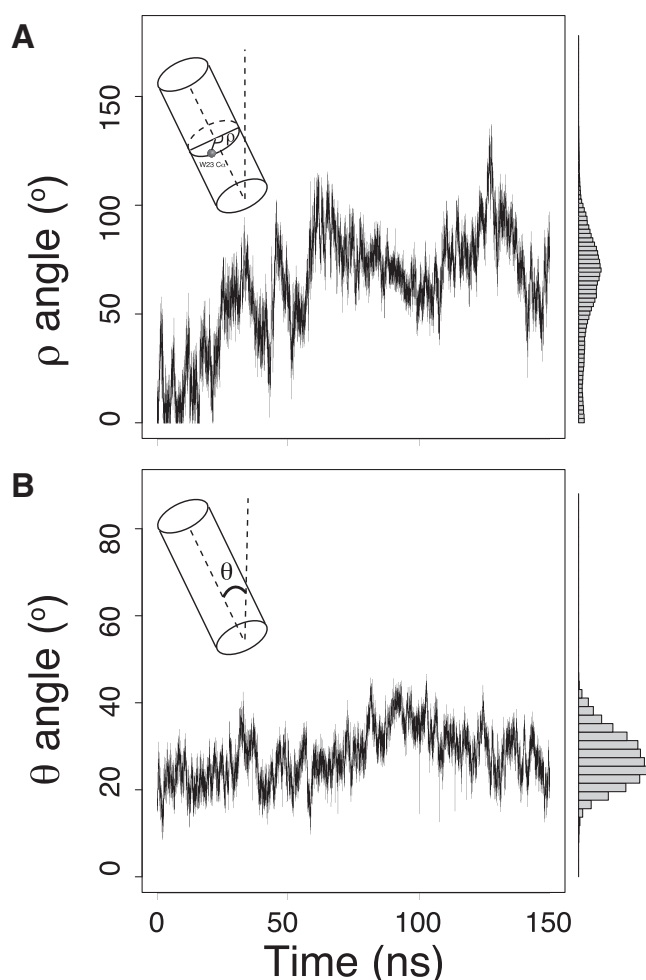


FIGURE 5 Time evolutions and distribution of the azimuthal (A) and tilt (B) angles for the entire SLN helix during MD simulations. Descriptions of the azimuthal angle, ρ , and tilt angle, θ , used for structural analysis are shown in the upper and lower insets, respectively.

~150-ns time evolution for the azimuthal angle. The initial value of the azimuthal angle is $\sim 20^\circ$. After 25 ns, there is a sharp transition and the angle continues to change monotonically up to an average value of 66° . In the last 100 ns of MD simulations, the azimuthal angle fluctuates around 66° . It is noteworthy that the motions of the N-terminal and C-terminal residues appear to drive the final topological arrangement of the protein. The change in the azimuthal angle is more clearly represented in Fig. 6, where the starting structure, the ending snapshot and the ideal helix model derived from PISEMA experiments are compared. The starting configuration of the MD calculations rotates $\sim 66^\circ$ to reach a configuration almost superimposable on that of the solid-state NMR model (17). In the initial configuration, two of the N-terminal hydrophobic residues (M1 and I3) are unfavorably placed near the polar headgroups, whereas the two C-terminal tyrosine residues are located in the bulk water phase. After 60 ns, these residues are embedded into the headgroup/hydrocarbon interface of the bilayer and

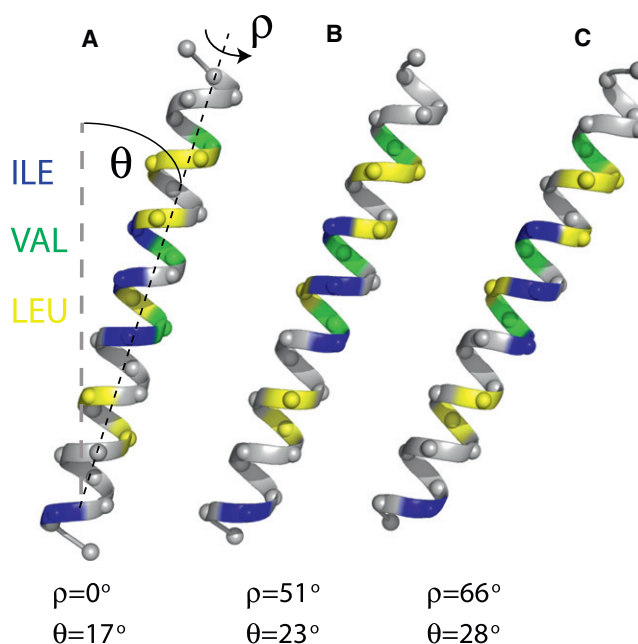


FIGURE 6 Structure comparison of the starting configuration (A), the ideal helix model best-fit PISEMA data (B), and the snapshot from the simulation having the average rotation and tilt angle (C). All C_α atoms are shown in spheres with the Ile, Val, and Leu residues colored blue, green, and yellow, respectively.

remain in this environment throughout the rest of the trajectory. These residues are known to be responsible for the SLN location in the sarcoplasmic reticulum membrane (92). The cation- π interaction between R27 and W23 occurs at ~ 50 ns, which is concomitant with the transition of the azimuthal angle from $\sim 20^\circ$ to $\sim 50^\circ$. This suggests that together with the hydrogen bonds formed by the N-terminus with the lipids, these cation- π interactions may constitute a driving force for SLN helix rotation. At the same time, the helical axis of SLN rotates to optimize the exposure of the most hydrophilic residue side chains (N4, T5, and N11) toward the lipid polar headgroups. In the last 100 ns of MD simulations, most of the polar residues of the N-terminus are anchored to the lipid headgroup region, forming electrostatic interactions to stabilize the SLN topology. The resulting azimuthal angle is in good agreement with the experimental results, with the face containing I3, L8, V15, L16, V19, and I26 pointing toward the sarcoplasmic reticulum lumen (17).

Analysis of fast backbone dynamics

The fast dynamics of the SLN backbone (on the picosecond to nanosecond timescale) was analyzed by calculating the generalized order parameter (S^2). Since the experimental data are not available for SLN in lipid bilayers, we compared the computed S^2 value with experimental values obtained in detergent micelles. The computed and experimental S^2 order parameters are compared in Fig. 7. Although there is good agreement among experimental and theoretical values for the helical region of SLN, our simulations show that the

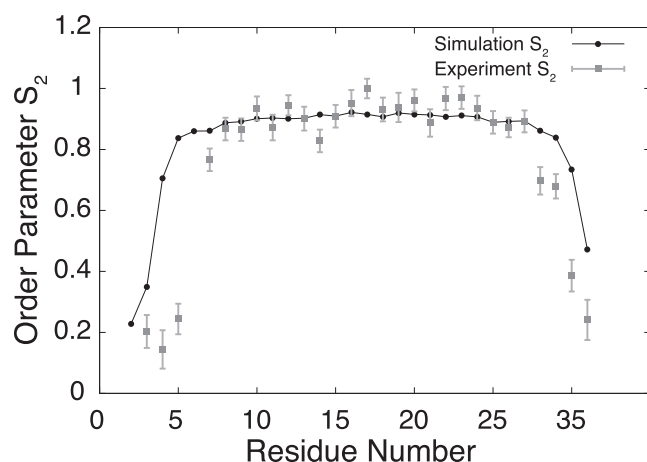


FIGURE 7 Comparison of the generalized order parameters (S^2) for the amide vectors of SLN obtained from MD simulations (black) and solution-NMR data in DPC micelles (gray).

terminal residues display higher S^2 values than the experimental data. Spin-relaxation data in detergent micelles revealed four different dynamics regions of SLN, mimicking the motions of the transmembrane domain of phospholamban (98), the SLN homolog in the cardiac muscle (53,54). The S^2 values obtained from MD simulations are more uniform, with an average value of 0.89 ± 0.04 from residues 5–30. For comparison, the experimental values show uniformity from residues 7–27 (0.91 ± 0.05). The slight difference between the calculated and experimental values may be attributed to the higher fluidity of the micellar environment causing higher fluctuations in the experiment compared with the lipid bilayers used in dynamics simulations. A

similar observation was made by Sansom and co-workers, who compared the dynamics of secondary-structure domains in both micellar systems and lipid bilayers (99). These researchers showed that the dynamic flexibility is greater in a micellar environment than in lipid bilayers, attributing the differences in mobility to the fast diffusion of detergent molecules and their reduced packing in the micellar core with respect to the lipid bilayers. Another important factor that may cause these discrepancies is the approximations used to calculate the electrostatic energy in the MD simulation and the lack of polarizable force field.

Analysis of the large-scale dynamics by PCA

The essential dynamics of SLN was determined using the protein configurations from the MD trajectories from 10 to 150 ns. These structures have been translated and superimposed with the initial (reference) structure to remove lateral diffusional motions. The backbone atoms from these configurations were rewritten into a new trajectory file in every 40-ps interval, with which the principal component analysis was performed using Bio3d (82). The first and second components (PC1 and PC2) represent the rotation of SLN around the helix axis and the dynamics of the tilt angle with respect to the lipid bilayer normal. The third component (PC3) features a smaller amplitude of rotation of SLN along the helix axis. PC1 has a larger N-terminal fluctuation than PC3. The first three principal components represent ~86% of the overall structural fluctuations of the entire protein during the MD simulations. In Fig. 8 A, we have projected the structures of the backbone atoms (N, H_N , $C\alpha$, C' , and O) in the MD trajectories onto the essential space (planes)

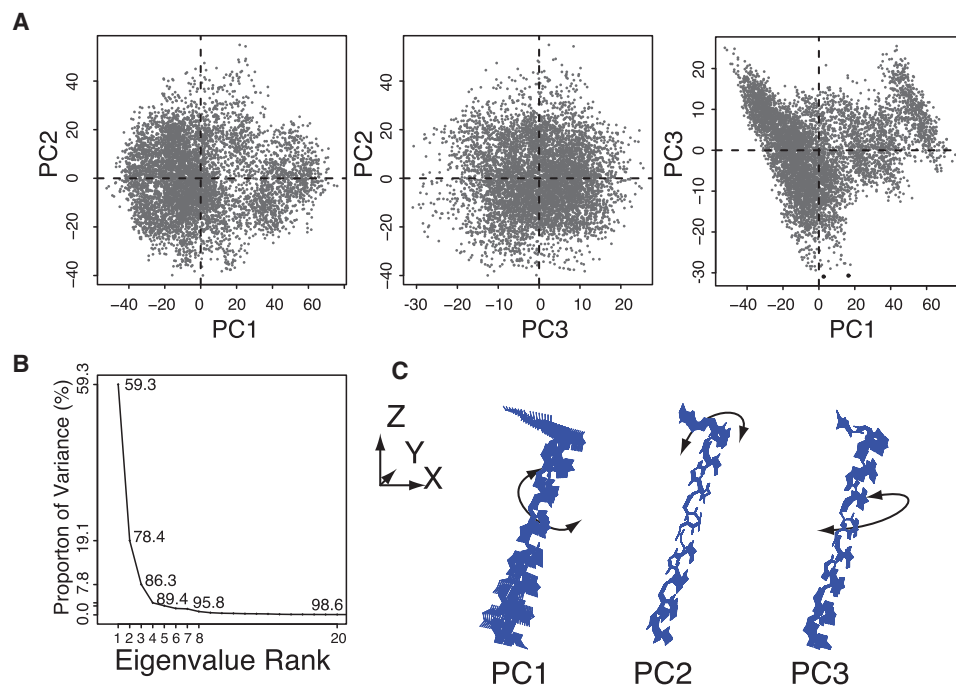


FIGURE 8 PCA of the backbone atoms of SLN for the last 40 ns of MD calculations. (A) Projection of PC1/PC2, PC2/PC3, and PC1/PC3 planes. (B) The cumulative contribution of the first 20 principal components to the overall structural variation. (C) Graphic representation of the first three principal components. The arrows indicate the direction of the structural fluctuations.

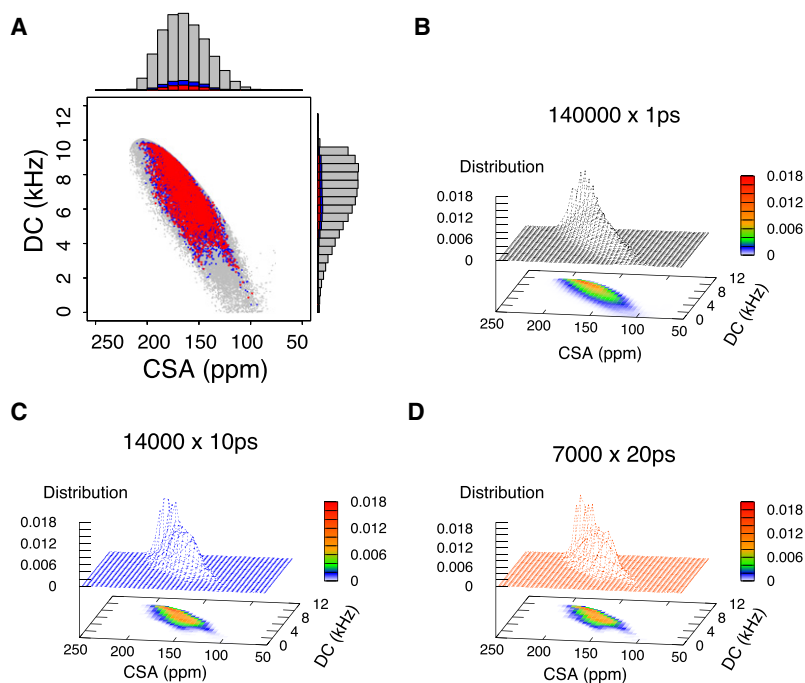


FIGURE 9 Simulated CSA and DC values obtained for residue 25 from MD trajectories of the last 140 ns of simulations. (A) Overlay of the calculated PISEMA spectra from SLN snapshots taken from MD trajectories. The distribution of the CSA and DC values is indicated on each axis. (B–D) Three-dimensional plot showing the distribution of CSA and DC for residue 25 with no torsion-angle averaging (B), with 10-ps torsion-angle averaging (C), and with 20-ps torsion-angle averaging (D).

defined by PC1/PC2, PC1/PC3, and PC2/PC3. This allows one to visualize the conformational space sampled during MD calculations. In the plots of Fig. 8 A, each point represents one conformation of SLN saved during the MD simulations, and the density of points is an indication of the population of conformations sampled in the molecular dynamics trajectory. The proportion of variance versus the eigenvalue rank (Fig. 8 B) clearly shows the relative importance of the different motions, with PC1 accounting for ~59%, PC2 for ~19%, and PC3 for only ~8% of the overall fluctuations. Since these results are based on 150 ns of MD simulations they only indicate the essential motions in the nanosecond timescale. Nevertheless, the PCA analysis provides a glimpse of the key features of the low-frequency large-amplitude motions of SLN in lipid bilayers.

Computation of the PISEMA spectra and the effect of dynamic averaging

To calculate the PISEMA spectra, we used the method described by Strauss and co-workers (45), where the CSA and DC values for each residue were back-calculated from SLN snapshots from the MD trajectories.

When the PISEMA spectra are calculated from instantaneous (snapshot) conformations of SLN sampled during every 1-ps interval during the MD simulation, each amide site gives rise to a wide distribution of both CSA and DC, as illustrated in Fig. 9 A. This has also been found in the simulation carried out by Straus and co-workers (45,46), who suggested that the fast motions of the amide vectors (libration, etc.) affect the appearance of the computed spectrum. The spread of the CSA and DC values around the

average values for each site approaches an anisotropic Gaussian distribution with a distinct maximum (Fig. 9 B). To illustrate the effects of fast motions involving the amide hydrogen, we performed a series of short-time averages of the out-of-plane torsion angle of the peptide plane at different time intervals, and we found that using this approach, it is possible to reduce the thermal noise caused by the fast dynamics of the amide vector during the MD simulations. Depicted in Fig. 9, C and D, are the results for residue 25 that were obtained using the average amide vector at 10- and 20-ps intervals, respectively. This short-time average of fast motions reduces the original data points (Fig. 9 B) from 140,000 to 14,000 (Fig. 9 C) and 7000 (Fig. 9 D) for 10- and 20-ps intervals, respectively. We found that conformation averaging over time periods >20 ps does not further narrow the distribution significantly.

The calculated PISEMA spectrum and the agreement between experimental and theoretical DC and CSA are shown in Fig. 10. The agreement between the experimental and calculated CSA and DC is good. However, the computed average CSA and DC values are somewhat smaller than those experimentally determined, corresponding to a larger tilt angle of SLN. The calculated PISEMA spectrum shows a distinct PISA wheel pattern, although the distribution of DC and CSA data around the average value is greater than the line widths obtained experimentally. The average standard deviations (error bars) between experiment and theory are 15.8 ± 4.2 ppm for CSA and 1.6 ± 0.4 kHz for DC. We also tested the agreement between experimental and calculated data using different CSA tensor values taken from the work of Wu et al. (84) (tensor 1), Straus et al. (45) (tensor 2), and Page et al. (10) (tensor 3). Fig. 11 shows

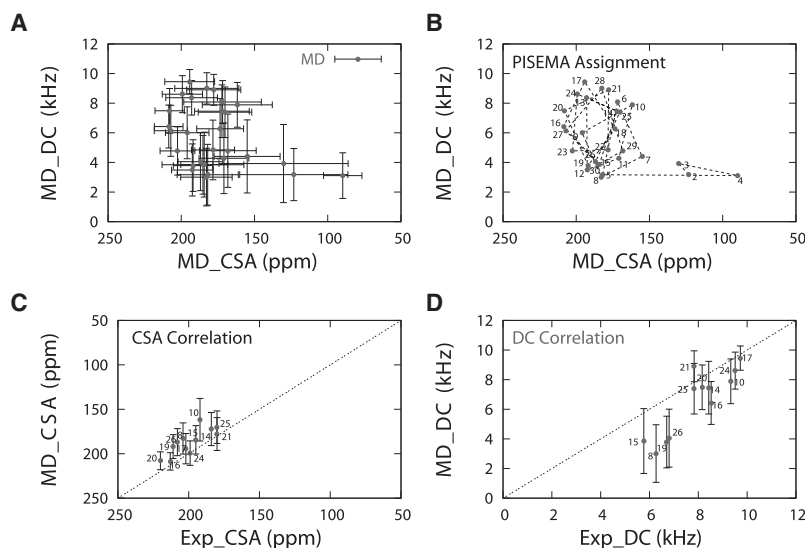


FIGURE 10 (A) Full PISEMA spectrum for all of the amide sites of SLN from the last 140 ns of the simulation using 10° torsion-angle averaging. Note that the error bars indicate the standard deviations of the values. (B) Average positions from A are shown, with labels corresponding to residue number. The resonances are connected using dotted lines to show the regular PISA wheel for the SLN helix. (C and D) Correlation of experimental and calculated CSA (C) and DC (D) for Leu, Ile, and Val only.

the calculation of the PISEMA patterns using the three tensors. The different values of the CSA tensors have little effect on the average CSA values calculated from the MD trajectories. As previously mentioned, the systematic deviations observed for both CSA and DC values from the experimental values could be due to the use of different lipids, hydration levels, etc. (i.e., bilayer thickness) in the experiments and in the MD simulations (94).

To understand the effects of slow motions on the calculated PISEMA spectra, we used PCA analysis to probe the low-frequency motions during the MD trajectories. Using the principal-component vectors, we projected the essential motions in the PISEMA plane. Fig. S1, A–D, in the [Supporting Material](#), shows the effects of the three main mode of motion as identified by the PCA analysis on the back-calculated PISEMA spectra. For clarity, we eliminated the

residues corresponding to the two termini, which are the most mobile, and focused on the analysis of the residues in the helical portion of the PISEMA spectra. The combination of the PCA components is reported in Fig. 12. We have also investigated the effects of mosaic spread (i.e., spatial distribution of conformations) on the PISEMA experiments. The mosaic spread was calculated using a uniform distribution of angles according to the method suggested by Cross and co-workers (44). We modeled the effects of spatial distribution around 4° , 10° , and 20° . It was interesting to find that the 10° mosaic spread (Fig. 12 B) would have an effect on the linewidths similar to that generated by the combined essential motions (PC1, PC2, and PC3 (Fig. 12 A)). This suggests that a spatial distribution of the polypeptide conformations $>10^\circ$ would be the dominating factor in the observable linewidths.

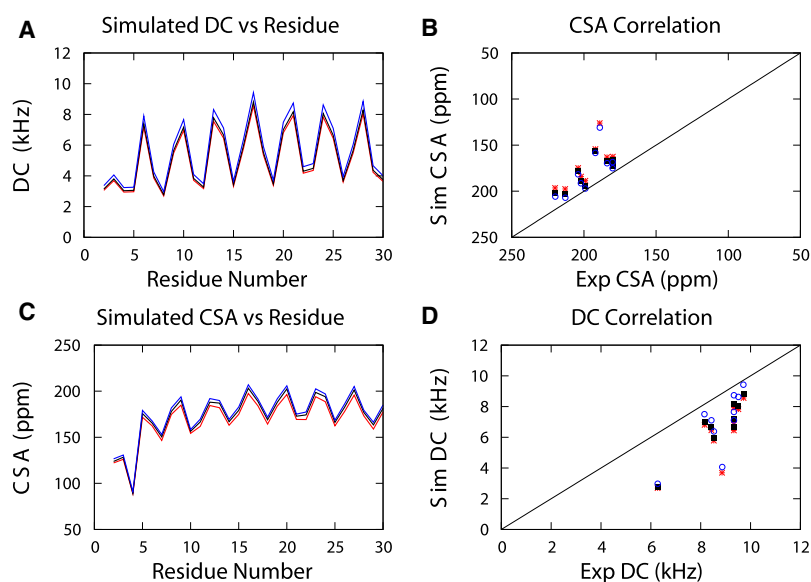


FIGURE 11 Effects of different values of the CSA tensors on the calculated PISEMA spectra. Values were obtained from Wu et al. (84) for tensor 1 (red), from Straus et al. (45) for tensor 2 (black), and from Page et al. (10) for tensor 3 (blue). Tensor 1, $\sigma_{11} = 64$, $\sigma_{22} = 77$, $\sigma_{33} = 217$, $\nu_{||} = 9.75$ kHz; tensor 2, $\sigma_{11} = 56.3$, $\sigma_{22} = 79$, $\sigma_{33} = 224$, $\nu_{||} = 10.05$ kHz; tensor 3, $\sigma_{11} = 57.3$, $\sigma_{22} = 81.2$, $\sigma_{33} = 228$, $\nu_{||} = 10.74$ kHz. Error bars are omitted for clarity.

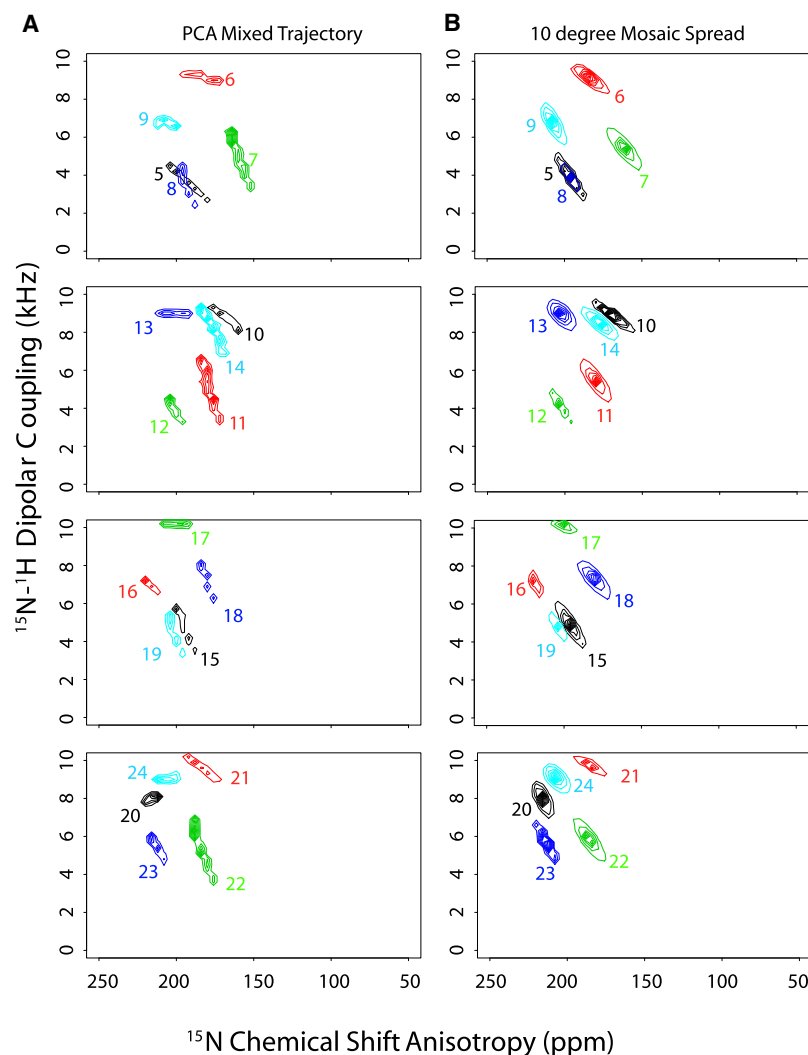


FIGURE 12 (A) Simulated contours of different residues using combined principal-component trajectories. (B) Simulated contour of 10° mosaic spread of protein orientation around the average position.

DISCUSSION

Molecular dynamics simulations at the molecular level have reached a state of sophistication such that it is possible to reproduce the physical chemical properties of proteins and membranes and, at the same time, to describe the details of protein-lipid interactions (100). In particular, MD calculations have been utilized to interpret and predict solid-state NMR parameters derived from membrane proteins reconstituted in oriented lipid bilayers such as ^2H quadrupolar couplings, ^{15}N and ^{13}C CSA and DC (63,101–104). For instance, Cross and co-workers applied a combined MD/NMR approach to obtain the first high-resolution structure of a membrane protein in lipid bilayers (105).

Subsequently, Roux and co-workers applied this combined MD/NMR approach to understand the structural dynamics of several other membrane proteins and peptides in various lipid environments (101,104). More recently, MD simulations have been used with success to study the structural dynamics and membrane interactions of antimicro-

bial peptides (106,107). From these studies emerged excellent agreements between experimental and calculated NMR parameters (CSA and DC), which made it possible to reproduce the topologies and lipid interactions of these membrane-embedded polypeptides.

Recent reports (47,48), however, have pointed out that dynamic averaging of ^2H quadrupolar couplings can cause substantial errors in the calculation of the tilt and azimuthal angles of small transmembrane peptides, suggesting that ^{15}N CSA and DC obtained from separated-local-field experiments would provide more accurate values of these angles. This view contrasts with a recent article from Koeppe and co-workers showing that the interpretation of ^{15}N CSA and DC and the quadrupolar couplings obtained from the GALA approach produce the same structural topology (49). However, protein dynamics affects the appearance of the NMR spectra. In a recent MD simulation study, Straus and co-workers concluded that dynamics affects the appearance and the interpretation of CSA and DC on both helical and β -barrel membrane proteins (45,46).

To analyze the effects of dynamic averaging on helical polypeptides, the dynamics of SLN were characterized using 150 ns of MD simulations in explicit DOPC lipid bilayer. This small membrane protein has been extensively studied in both SDS and DPC micelles (7,52). In addition, its topological orientation (tilt and azimuthal angles) was determined in DOPC/DOPE lipid bilayers by solid-state NMR (17). From the analysis of the MD trajectories, we found that SLN maintains its helical conformation throughout the simulations, with both termini adopting a more helical structure than experimentally observed in both DPC and SDS (7,52). This can be attributed to the membrane environment that stabilizes the SLN secondary structure more than the micellar environment does. This prediction awaits for an experimental validation.

It was interesting to find that T13 and T18 are positioned in the hydrocarbon region of the membrane bilayers. In the monomeric form of SLN that we have studied by MD simulations, these residues are hydrogen-bonded with the polypeptide backbone for SLN. However, they might be crucial for SLN oligomerization at high protein/lipid ratios (108) and for ion-conducting activity we recently measured in mercury-supported lipid bilayers (109). Taken with previous studies on micelles and liposomes (108), these data support the hypothesis that SLN is able to form ion-conducting pores permeable to small inorganic anions such as chloride, phosphate, or sulfate and impermeable to cations such as sodium and potassium (109).

The topology of SLN converges and oscillates around average values that are in close agreement with those determined using solid-state NMR. If the main driving force for SLN solubilization by the lipid bilayer is the hydrophobic mismatch, these simulations clearly show that both the N- and C-terminal residues determine the rotation (azimuthal) angle. These conclusions agree with previous work carried out by Di Nola and colleagues with model membrane proteins embedded in implicit membrane environments (110). However, simulations in explicit membrane environment converge into a slightly different topology for SLN. Previous studies using Monte Carlo folding and an implicit generalized Born membrane reported that SLN is less helical with a tilt angle of $16 \pm 8^\circ$ (111). Indeed, using CHARMM and implicit model membranes, we obtained approximately the same result ($\theta = 17 \pm 6^\circ$). In a similar way, Brooks and co-workers found for the fd coat protein only a semi-quantitative agreement between solid-state NMR data and MD simulations when using replica-exchange molecular dynamics and the implicit-membrane generalized Born model (112). In that work, the simulations of SLN in explicit DOPC bilayer resulted in tilt and azimuthal angles in closer accord with those determined experimentally. This emphasizes the importance of specific interactions between the explicit lipid membrane and SLN.

In agreement with a previous MD study by Straus and co-workers (45), our simulations show that fast dynamics

(on the picosecond to nanosecond timescale) of the amide backbone sites dramatically affects the appearance of back-calculated PISEMA spectra, resulting in broad distributions of peaks, which makes it difficult to observe regular PISA wheels (45). These fast fluctuations involving the amide hydrogen (such as amide libration motion) are more rapid than the time resolution of the PISEMA experiments. We found that the fast fluctuations can be largely filtered out by averaging the torsion angle of the amide out-of-plane mode over 10- to 20-ps intervals along the MD trajectory. As a result, it is possible to match the experimental results and obtain reasonably regular oscillatory patterns for both CSA and DC (i.e., the PISA wheel).

To understand the effects of the low-frequency, large-amplitude motions characterized by essential component motions, we projected the PC1, PC2, and PC3 trajectories onto the PISEMA spectra. We found that these slow dynamical modes have a pronounced effect on the back-calculated values of DC and CSA values, exhibiting narrower spectral lines than those obtained from the full dynamics. As for the fast amide-vector dynamics, these motions are also much faster than the timescale of the PISEMA experiments, which are also averaged out under experimental conditions (i.e., slow and fast dynamics are rapid compared to the time resolution of the PISEMA experiment). We also compared the effects of protein dynamics with the mosaic spread. For SLN, we concluded that a spatial distribution of conformations of $>10^\circ$ would dominate the observable linewidths.

Although both dynamics and spatial distribution affect the linewidths, the average values computed by CSA and DC for SLN oscillate with 3.6 periodicity according to its helical conformation (30,83,113,114). It is noteworthy that the slight bend that the MD predicts for SLN causes a slight deviation in the wheel pattern (Fig. 10) at residues 7–14, whereas residues 15–26 follow the canonical PISA wheel with a pitch of ~ 3.6 residues per turn. This indicates that the most rigid portion of SLN on average assumes a helical conformation that is close to ideal. This is in agreement with the uniformity and ideality of strongly hydrogen-bonded transmembrane polypeptides proposed by Cross and co-workers (15,115).

CONCLUSIONS

In conclusion, the MD simulations of SLN in explicit DOPC lipid membranes show that the topology of this small transmembrane protein converges to that experimentally determined by solid-state NMR in oriented lipid bilayers, with similar tilt and azimuthal (rotational) angles. From the MD trajectories, it is possible to back-calculate PISEMA spectra (CSA and DC for each amide site), which are in good agreement with the experimental results. The fast and slow motions (picosecond to millisecond) are rapid compared to the time resolution of the PISEMA experiment, and are

averaged out. As a consequence, the back-calculated spectra of the helical portion of SLN from the MD trajectory reveal the classical PISA wheel pattern. This demonstrates that MD trajectories can reproduce the topology of single-pass membrane proteins and can be used to predict and help in the interpretation of solid-state NMR data.

SUPPORTING MATERIAL

One figure is available at [http://www.biophysj.org/biophysj/supplemental/S0006-3495\(09\)00581-5](http://www.biophysj.org/biophysj/supplemental/S0006-3495(09)00581-5).

The authors thank Dr. Nathaniel Traaseth, Dr. Jarrod Buffry, Dr. Tata Gopinath, and Prof. R. Guidelli for many helpful discussions. This work was carried out in part using hardware and software provided by the University of Minnesota Supercomputing Institute.

This work was supported by National Institutes of Health grants GM64742, GM072701, and HL080081 to G.V. and GM46736 to J.G.

REFERENCES

- Wallin, E., and G. von Heijne. 1998. Genome-wide analysis of integral membrane proteins from eubacterial, archaean, and eukaryotic organisms. *Protein Sci.* 7:1029–1038.
- White, S. H., and G. von Heijne. 2004. The machinery of membrane protein assembly. *Curr. Opin. Struct. Biol.* 14:397–404.
- Pervushin, K., R. Riek, G. Wider, and K. Wuthrich. 1997. Attenuated T2 relaxation by mutual cancellation of dipole-dipole coupling and chemical shift anisotropy indicates an avenue to NMR structures of very large biological macromolecules in solution. *Proc. Natl. Acad. Sci. USA.* 94:12366–12371.
- Tamm, L. K., and B. Liang. 2006. NMR of membrane proteins in solution. *Prog. Nucl. Magn. Reson. Spectrosc.* 48:201–210.
- Zamoon, J., F. Nitu, C. Karim, D. D. Thomas, and G. Veglia. 2005. Mapping the interaction surface of a membrane protein: unveiling the conformational switch of phospholamban in calcium pump regulation. *Proc. Natl. Acad. Sci. USA.* 102:4747–4752.
- Traaseth, N. J., D. D. Thomas, and G. Veglia. 2006. Effects of Ser¹⁶ phosphorylation on the allosteric transitions of phospholamban/Ca²⁺-ATPase complex. *J. Mol. Biol.* 358:1041–1050.
- Buffry, J. J., B. A. Buck-Koehntop, F. Porcelli, N. J. Traaseth, D. D. Thomas, et al. 2006. Defining the intramembrane binding mechanism of sarcolipin to calcium ATPase using solution NMR spectroscopy. *J. Mol. Biol.* 358:420–429.
- Ha, K. N., N. J. Traaseth, R. Verardi, J. Zamoon, A. Cembran, et al. 2007. Controlling the inhibition of the sarcoplasmic Ca²⁺-ATPase by tuning phospholamban structural dynamics. *J. Biol. Chem.* 282:37205–37214.
- Opella, S. J., and F. M. Marassi. 2004. Structure determination of membrane proteins by NMR spectroscopy. *Chem. Rev.* 104:3587–3606.
- Page, R. C., S. Kim, and T. A. Cross. 2008. Transmembrane helix uniformity examined by spectral mapping of torsion angles. *Structure.* 16:787–797.
- Baldus, M. 2007. Magnetic resonance in the solid state: applications to protein folding, amyloid fibrils and membrane proteins. *Eur. Biophys. J.* 36(Suppl 1):S37–S48.
- Hong, M. 2006. Oligomeric structure, dynamics, and orientation of membrane proteins from solid-state NMR. *Structure.* 14:1731–1740.
- Gong, X. M., C. M. Franzin, K. Thai, J. Yu, and F. M. Marassi. 2007. Nuclear magnetic resonance structural studies of membrane proteins in micelles and bilayers. *Methods Mol. Biol.* 400:515–529.
- Durr, U. H., L. Waskell, and A. Ramamoorthy. 2007. The cytochromes P450 and b5 and their reductases—promising targets for structural studies by advanced solid-state NMR spectroscopy. *Biochim. Biophys. Acta.* 1768:3235–3259.
- Page, R. C., C. Li, J. Hu, F. P. Gao, and T. A. Cross. 2007. Lipid bilayers: an essential environment for the understanding of membrane proteins. *Magn. Reson. Chem.* 45:S2–S11.
- Ramamoorthy, A., S. Thennarasu, D. K. Lee, A. Tan, and L. Maloy. 2006. Solid-state NMR investigation of the membrane-disrupting mechanism of antimicrobial peptides MSI-78 and MSI-594 derived from magainin 2 and melittin. *Biophys. J.* 91:206–216.
- Buffry, J. J., N. J. Traaseth, A. Mascioni, P. L. Gor'kov, E. Y. Chekmenev, et al. 2006. Two-dimensional solid-state NMR reveals two topologies of sarcolipin in oriented lipid bilayers. *Biochemistry.* 45:10939–10946.
- Traaseth, N. J., J. J. Buffry, J. Zamoon, and G. Veglia. 2006. Structural dynamics and topology of phospholamban in oriented lipid bilayers using multidimensional solid-state NMR. *Biochemistry.* 45:13827–13834.
- Park, S. H., A. A. Mrse, A. A. Nevzorov, M. F. Mesleh, M. Oblatt-Montal, et al. 2003. Three-dimensional structure of the channel-forming trans-membrane domain of virus protein “u” (vpu) from HIV-1. *J. Mol. Biol.* 333:409–424.
- Teriete, P., C. M. Franzin, J. Choi, and F. M. Marassi. 2007. Structure of the Na,K-ATPase regulatory protein FXYD1 in micelles. *Biochemistry.* 46:6774–6783.
- Traaseth, N. J., R. Verardi, K. D. Torgersen, C. B. Karim, D. D. Thomas, et al. 2007. Spectroscopic validation of the pentameric structure of phospholamban. *Proc. Natl. Acad. Sci. USA.* 104:14676–14681.
- Hu, J., T. Asbury, S. Achuthan, C. Li, R. Bertram, et al. 2007. Backbone structure of the amantadine-blocked trans-membrane domain M2 proton channel from influenza A virus. *Biophys. J.* 92:4335–4343.
- De Angelis, A. A., S. C. Howell, A. A. Nevzorov, and S. J. Opella. 2006. Structure determination of a membrane protein with two trans-membrane helices in aligned phospholipid bicelles by solid-state NMR spectroscopy. *J. Am. Chem. Soc.* 128:12256–12267.
- Park, S. H., S. Prytulla, A. A. De Angelis, J. M. Brown, H. Kiefer, et al. 2006. High-resolution NMR spectroscopy of a GPCR in aligned bicelles. *J. Am. Chem. Soc.* 128:7402–7403.
- van der Wel, P. C., E. Strandberg, J. A. Killian, and R. E. Koeppe, 2nd. 2002. Geometry and intrinsic tilt of a tryptophan-anchored transmembrane α -helix determined by ²H NMR. *Biophys. J.* 83:1479–1488.
- Strandberg, E., P. Wadhvani, P. Tremouilhac, U. H. Durr, and A. S. Ulrich. 2006. Solid-state NMR analysis of the PGLa peptide orientation in DMPC bilayers: structural fidelity of ²H-labels versus high sensitivity of 19F-NMR. *Biophys. J.* 90:1676–1686.
- Glaser, R. W., C. Sachse, U. H. Durr, P. Wadhvani, S. Afonin, et al. 2005. Concentration-dependent realignment of the antimicrobial peptide PGLa in lipid membranes observed by solid-state 19F-NMR. *Biophys. J.* 88:3392–3397.
- Mesleh, M. F., S. Lee, G. Veglia, D. S. Thiriot, F. M. Marassi, et al. 2003. Dipolar waves map the structure and topology of helices in membrane proteins. *J. Am. Chem. Soc.* 125:8928–8935.
- Mesleh, M. F., G. Veglia, T. M. DeSilva, F. M. Marassi, and S. J. Opella. 2002. Dipolar waves as NMR maps of protein structure. *J. Am. Chem. Soc.* 124:4206–4207.
- Mascioni, A., and G. Veglia. 2003. Theoretical analysis of residual dipolar coupling patterns in regular secondary structures of proteins. *J. Am. Chem. Soc.* 125:12520–12526.
- Mascioni, A., B. L. Eggimann, and G. Veglia. 2004. Determination of helical membrane protein topology using residual dipolar couplings and exhaustive search algorithm: application to phospholamban. *Chem. Phys. Lipids.* 132:133–144.
- Wang, J., J. D. Walsh, J. Kuszewski, and Y. X. Wang. 2007. Periodicity, planarity, and pixel (3P): a program using the intrinsic residual dipolar coupling periodicity-to-peptide plane correlation and ϕ/ψ angles to derive protein backbone structures. *J. Magn. Reson.* 189:90–103.

33. Bouvignies, G., P. R. Markwick, and M. Blackledge. 2008. Characterization of protein dynamics from residual dipolar couplings using the three dimensional Gaussian axial fluctuation model. *Proteins*. 71:353–363.
34. Salvatella, X., B. Richter, and M. Vendruscolo. 2008. Influence of the fluctuations of the alignment tensor on the analysis of the structure and dynamics of proteins using residual dipolar couplings. *J. Biomol. NMR*. 40:71–81.
35. Markwick, P. R., G. Bouvignies, and M. Blackledge. 2007. Exploring multiple timescale motions in protein GB3 using accelerated molecular dynamics and NMR spectroscopy. *J. Am. Chem. Soc.* 129:4724–4730.
36. Bouvignies, G., P. Markwick, R. Bruschweiler, and M. Blackledge. 2006. Simultaneous determination of protein backbone structure and dynamics from residual dipolar couplings. *J. Am. Chem. Soc.* 128:15100–15101.
37. Lakomek, N. A., T. Carlomagno, S. Becker, C. Griesinger, and J. Meiler. 2006. A thorough dynamic interpretation of residual dipolar couplings in ubiquitin. *J. Biomol. NMR*. 34:101–115.
38. Ryabov, Y., and D. Fushman. 2006. Analysis of interdomain dynamics in a two-domain protein using residual dipolar couplings together with ¹⁵N relaxation data. *Magn. Reson. Chem.* 44 Spec. No:S143–S151.
39. Tolman, J. R., and K. Ruan. 2006. NMR residual dipolar couplings as probes of biomolecular dynamics. *Chem. Rev.* 106:1720–1736.
40. Blackledge, M. 2005. Recent progress in the study of biomolecular structure and dynamics in solution from residual dipolar couplings. *Prog. Nucl. Magn. Reson. Spectrosc.* 46:23–61.
41. Bax, A. 2003. Weak alignment offers new NMR opportunities to study protein structure and dynamics. *Protein Sci.* 12:1–16.
42. Tolman, J. R., H. M. Al-Hashimi, L. E. Kay, and J. H. Prestegard. 2001. Structural and dynamic analysis of residual dipolar coupling data for proteins. *J. Am. Chem. Soc.* 123:1416–1424.
43. Fischer, M. W. F., J. A. Losonczi, J. L. Weaver, and J. H. Prestegard. 1999. Domain orientation and dynamics in multidomain proteins from residual dipolar couplings. *Biochemistry*. 38:9013–9022.
44. Quine, J. R., S. Achuthan, T. Asbury, R. Bertram, M. S. Chapman, et al. 2006. Intensity and mosaic spread analysis from PISEMA tensors in solid-state NMR. *J. Magn. Reson.* 179:190–198.
45. Straus, S. K., W. R. Scott, and A. Watts. 2003. Assessing the effects of time and spatial averaging in ¹⁵N chemical shift/¹⁵N-¹H dipolar correlation solid state NMR experiments. *J. Biomol. NMR*. 26:283–295.
46. Bleile, D. W., W. R. Scott, and S. K. Straus. 2005. Can PISEMA experiments be used to extract structural parameters for mobile β -barrels? *J. Biomol. NMR*. 32:101–111.
47. Ozdirekcan, S., C. Etchebest, J. A. Killian, and P. F. Fuchs. 2007. On the orientation of a designed transmembrane peptide: toward the right tilt angle? *J. Am. Chem. Soc.* 129:15174–15181.
48. Esteban-Martin, S., and J. Salgado. 2007. The dynamic orientation of membrane-bound peptides: bridging simulations and experiments. *Biophys. J.* 93:4278–4288.
49. Vostrikov, V. V., C. V. Grant, A. E. Daily, S. J. Opella, and R. E. Koeppe, 2nd. 2008. Comparison of “polarization inversion with spin exchange at magic angle” and “geometric analysis of labeled alanines” methods for transmembrane helix alignment. *J. Am. Chem. Soc.* 130:12584–12585.
50. Buck, B., J. Zamoan, T. L. Kirby, T. M. DeSilva, C. Karim, et al. 2003. Overexpression, purification, and characterization of recombinant Ca-ATPase regulators for high-resolution solution and solid-state NMR studies. *Protein Expr. Purif.* 30:253–261.
51. Traaseth, N. J., K. N. Ha, R. Verardi, L. Shi, J. J. Buffy, et al. 2008. Structural and dynamic basis of phospholamban and sarcolipin inhibition of Ca²⁺-ATPase. *Biochemistry*. 47:3–13.
52. Mascioni, A., C. Karim, G. Barany, D. D. Thomas, and G. Veglia. 2002. Structure and orientation of sarcolipin in lipid environments. *Biochemistry*. 41:475–482.
53. Mac Lennan, D. H., and E. G. Kranias. 2003. Phospholamban: a crucial regulator of cardiac contractility. *Natl. Rev.* 4:566–577.
54. Periasamy, M., and A. Kalyanasundaram. 2007. SERCA pump isoforms: their role in calcium transport and disease. *Muscle Nerve*. 35:430–442.
55. Ramamoorthy, A., Y. Wei, and L. Dong-Kuk. 2004. PISEMA solid-state NMR spectroscopy. *Annu. Rep. NMR Spectrosc.* 52:1–52.
56. Lomize, M. A., A. L. Lomize, I. D. Pogozheva, and H. I. Mosberg. 2006. OPM: orientations of proteins in membranes database. *Bioinformatics*. 22:623–625.
57. Im, W., M. Feig, and C. L. Brooks, 3rd. 2003. An implicit membrane generalized born theory for the study of structure, stability, and interactions of membrane proteins. *Biophys. J.* 85:2900–2918.
58. Tristram-Nagle, S., H. I. Petrache, and J. F. Nagle. 1998. Structure and interactions of fully hydrated dioleoylphosphatidylcholine bilayers. *Biophys. J.* 75:917–925.
59. Costigam, S. C., P. J. Booth, and R. H. Templer. 2000. Estimations of lipid bilayer geometry in fluid lamellar phases. *Biochim. Biophys. Acta*. 1468:41–54.
60. Brooks, B. R., R. E. Bruccoleri, B. D. Olafson, D. J. States, S. Swaminathan, et al. 1983. CHARMM: a program for macromolecular energy, minimization, and dynamics calculations. *J. Comput. Chem.* 4: 187–217.
61. MacKerell, A. D., D. Bashford, M. Bellott, R. L. Dunbrack, J. D. Evanseck, et al. 1998. All-atom empirical potential for molecular modeling and dynamics studies of proteins. *J. Phys. Chem. B*. 102:3586–3616.
62. Mackerell, Jr., A. D. 2004. Empirical force fields for biological macromolecules: overview and issues. *J. Comput. Chem.* 25:1584–1604.
63. Mackerell, Jr., A. D., M. Feig, and C. L. Brooks, 3rd. 2004. Extending the treatment of backbone energetics in protein force fields: limitations of gas-phase quantum mechanics in reproducing protein conformational distributions in molecular dynamics simulations. *J. Comput. Chem.* 25:1400–1415.
64. Woolf, T. B., and B. Roux. 1996. Structure, energetics, and dynamics of lipid-protein interactions: a molecular dynamics study of the gramicidin A channel in a DMPC bilayer. *Proteins*. 24:92–114.
65. Woolf, T. B., and B. Roux. 1994. Molecular dynamics simulation of the gramicidin channel in a phospholipid bilayer. *Proc. Natl. Acad. Sci. USA*. 91:11631–11635.
66. Lewis, B. A., and D. M. Engelman. 1983. Lipid bilayer thickness varies linearly with acyl chain length in fluid phosphatidylcholine vesicles. *J. Mol. Biol.* 166:211–217.
67. Lewis, B. A., and D. M. Engelman. 1983. Bacteriorhodopsin remains dispersed in fluid phospholipid bilayers over a wide range of bilayer thicknesses. *J. Mol. Biol.* 166:203–210.
68. Jorgensen, W. L., J. Chandrasekhar, J. D. Madura, R. W. Impey, and M. L. Klein. 1983. Comparison of simple potential functions for simulating liquid water. *J. Chem. Phys.* 79:926–935.
69. Ryckaert, J.-P., G. Ciccotti, and H. J. C. Berendsen. 1977. Numerical integration of the Cartesian equations of motion of a system with constraints: molecular dynamics of *n*-alkanes. *J. Comput. Phys.* 23:327–341.
70. Renner, P., C. G. Caratsch, P. G. Waser, P. Lazarovici, and N. Primor. 1987. Presynaptic effects of the pardaxins, polypeptides isolated from the gland secretion of the flatfish *Pardachirus marmoratus*. *Neuroscience*. 23:319–325.
71. Essmann, U., L. Perera, M. L. Berkowitz, T. Darden, H. Lee, et al. 1995. A smooth particle mesh Ewald method. *J. Chem. Phys.* 103:8577–8593.
72. Sagui, C., and T. A. Darden. 1999. Molecular dynamics simulations of biomolecules: long-range electrostatic effects. *Annu. Rev. Biophys. Biomol. Struct.* 28:155–179.
73. Dufourcq, J., J. F. Faucon, G. Fourche, J. L. Dasseux, M. Le Marie, et al. 1986. Morphological changes of phosphatidylcholine bilayers induced by melittin: vesicularization, fusion, discoidal particles. *Biochim. Biophys. Acta*. 859:33–48.

74. Buckling, A., and M. Brockhurst. 2005. Microbiology: RAMP resistance. *Nature*. 438:170–171.
75. Matsuzaki, K. 2001. Why and how are peptide-lipid interactions utilized for self defence? *Biochem. Soc. Trans.* 29:598–601.
76. Hara, T., H. Kodama, M. Kondo, K. Wakamatsu, A. Takeda, et al. 2001. Effects of peptide dimerization on pore formation: antiparallel disulfide-dimerized magainin 2 analogue. *Biopolymers*. 58:437–446.
77. Lipari, G., and A. Szabo. 1982. Model-free approach to the interpretation of nuclear magnetic resonance relaxation in macromolecules. 1. Theory and range of validity. *J. Am. Chem. Soc.* 104:4546–4559.
78. Cole, R., and J. P. Loria. 2003. FAST-modelfree: A program for rapid automated analysis of solution NMR spin-relaxation data. *J. Biomol. NMR*. 26:203–213.
79. Mandel, A. M., M. Akke, and A. G. Palmer. 1995. Backbone dynamics of *Escherichia coli* ribonuclease HI: correlations with structure and function in an active enzyme. *J. Mol. Biol.* 246:144–163.
80. Garcia, A. E. 1992. Large-amplitude nonlinear motions in proteins. *Phys. Rev. Lett.* 68:2696–2699.
81. Clarage, J. B., T. Romo, B. K. Andrews, B. M. Pettitt, and G. N. Phillips, Jr. 1995. A sampling problem in molecular dynamics simulations of macromolecules. *Proc. Natl. Acad. Sci. USA*. 92:3288–3292.
82. Grant, B. J., A. P. Rodrigues, K. M. El Sawy, J. A. McCammon, and L. S. Caves. 2006. Bio3d: an R package for the comparative analysis of protein structures. *Bioinformatics*. 22:2695–2696.
83. Denny, J. K., J. Wang, T. A. Cross, and J. R. Quine. 2001. PISEMA powder patterns and PISA wheels. *J. Magn. Reson.* 152:217–226.
84. Wu, C. H., A. Ramamoorthy, L. M. Geirasch, and S. J. Opella. 1995. Simultaneous characterization of the amide ^1H chemical shift, ^1H - ^{15}N dipolar, and ^{15}N chemical shift interaction tensor in a peptide bond by three-dimensional solid-state NMR spectroscopy. *J. Am. Chem. Soc.* 117:6148–6149.
85. Wiener, M. C., and S. H. White. 1992. Structure of a fluid dioleoyl-phosphatidylcholine bilayer determined by joint refinement of x-ray and neutron diffraction data. II. Distribution and packing of terminal methyl groups. *Biophys. J.* 61:428–433.
86. Wimley, W. C., and S. H. White. 1996. Experimentally determined hydrophobicity scale for proteins at membrane interfaces. *Nat. Struct. Biol.* 3:842–848.
87. Gramolini, A. O., M. G. Trivieri, G. Y. Oudit, T. Kislinger, W. Li, et al. 2006. Cardiac-specific overexpression of sarcolipin in phospholamban null mice impairs myocyte function that is restored by phosphorylation. *Proc. Natl. Acad. Sci. USA*. 103:2446–2451.
88. Johansson, A. C., and E. Lindahl. 2006. Amino-acid solvation structure in transmembrane helices from molecular dynamics simulations. *Biophys. J.* 91:4450–4463.
89. White, S. H., W. C. Wimley, A. S. Ladokhin, and K. Hristova. 1998. Protein folding in membranes: determining energetics of peptide-bilayer interactions. *Methods Enzymol.* 295:62–87.
90. White, S. H., and W. C. Wimley. 1999. Membrane protein folding and stability: physical principles. *Annu. Rev. Biophys. Biomol. Struct.* 28:319–365.
91. Petersen, F. N., M. O. Jensen, and C. H. Nielsen. 2005. Interfacial tryptophan residues: a role for the cation- π effect? *Biophys. J.* 89:3985–3996.
92. Gramolini, A. O., T. Kislinger, M. Asahi, W. Li, A. Emili, et al. 2004. Sarcolipin retention in the endoplasmic reticulum depends on its C-terminal RSYQY sequence and its interaction with sarco(endo)plasmic Ca^{2+} -ATPases. *Proc. Natl. Acad. Sci. USA*. 101:16807–16812.
93. Aqvist, J. 1986. A simple way to calculate the axis of an α -helix. *Comput. Chem.* 10:97–99.
94. Rostovtseva, T. K., H. I. Petrache, N. Kazemi, E. Hassanzadeh, and S. M. Bezrukov. 2008. Interfacial polar interactions affect gramicidin channel kinetics. *Biophys. J.* 94:L23–L25.
95. Park, S. H., and S. J. Opella. 2005. Tilt angle of a trans-membrane helix is determined by hydrophobic mismatch. *J. Mol. Biol.* 350:310–318.
96. Harzer, U., and B. Bechinger. 2000. Alignment of lysine-anchored membrane peptides under conditions of hydrophobic mismatch: A CD, N-15 and P-31 solid state NMR spectroscopy investigation. *Biochemistry*. 39:13106–13144.
97. Marassi, F. M., and S. J. Opella. 2000. A solid-state NMR index of helical membrane protein structure and topology. *J. Magn. Reson.* 144:150–155.
98. Metcalfe, E. E., J. Zamoan, D. D. Thomas, and G. Veglia. 2004. $^1\text{H}/^{15}\text{N}$ heteronuclear NMR spectroscopy shows four dynamic domains for phospholamban reconstituted in dodecylphosphocholine micelles. *Biophys. J.* 87:1205–1214.
99. Bond, P. J., and M. S. Sansom. 2003. Membrane protein dynamics versus environment: simulations of OmpA in a micelle and in a bilayer. *J. Mol. Biol.* 329:1035–1053.
100. Tobias, T. J., K. C. Tu, and M. Klein. 1997. Atomic-scale molecular dynamics simulations of lipid membranes. *Curr. Opin. Colloid Interface Sci.* 2:15–26.
101. Berneche, S., M. Nina, and B. Roux. 1998. Molecular dynamics simulation of melittin in a dimyristoylphosphatidylcholine bilayer membrane. *Biophys. J.* 75:1603–1618.
102. Allen, T. W., O. S. Andersen, and B. Roux. 2003. Structure of gramicidin A in a lipid bilayer environment determined using molecular dynamics simulations and solid-state NMR data. *J. Am. Chem. Soc.* 125:9868–9877.
103. Ketchum, R., B. Roux, and T. Cross. 1997. High-resolution polypeptide structure in a lamellar phase lipid environment from solid state NMR derived orientational constraints. *Structure*. 5:1655–1669.
104. Woolf, T. B., and B. Roux. 1997. The binding site of sodium in the gramicidin A channel: comparison of molecular dynamics with solid-state NMR data. *Biophys. J.* 72:1930–1945.
105. Ketchum, R. R., W. Hu, and T. A. Cross. 1993. High-resolution conformation of gramicidin A in a lipid bilayer by solid-state NMR. *Science*. 261:1457–1460.
106. Ramamoorthy, A., S. K. Kandasamy, D. K. Lee, S. Kidambi, and R. G. Larson. 2007. Structure, topology, and tilt of cell-signaling peptides containing nuclear localization sequences in membrane bilayers determined by solid-state NMR and molecular dynamics simulation studies. *Biochemistry*. 46:965–975.
107. Sternberg, U., R. Witter, and A. S. Ulrich. 2007. All-atom molecular dynamics simulations using orientational constraints from anisotropic NMR samples. *J. Biomol. NMR*. 38:23–39.
108. Hellstern, S., S. Pegoraro, C. B. Karim, A. Lustig, D. D. Thomas, et al. 2001. Sarcolipin, the shorter homologue of phospholamban, forms oligomeric structures in detergent micelles and in liposomes. *J. Biol. Chem.* 276:30845–30852.
109. Becucci, L., R. Guidelli, C. B. Karim, D. D. Thomas, and G. Veglia. 2007. An electrochemical investigation of sarcolipin reconstituted into a mercury-supported lipid bilayer. *Biophys. J.* 93:2678–2687.
110. Ulmschneider, M. B., J. P. Ulmschneider, M. S. Sansom, and A. Di Nola. 2007. A generalized Born implicit-membrane representation compared to experimental insertion free energies. *Biophys. J.* 92:2338–2349.
111. Ulmschneider, J. P., M. B. Ulmschneider, and A. Di Nola. 2007. Monte Carlo folding of trans-membrane helical peptides in an implicit generalized Born membrane. *Proteins*. 69:297–308.
112. Im, W., and C. L. Brooks, 3rd. 2004. De novo folding of membrane proteins: an exploration of the structure and NMR properties of the fd coat protein. *J. Mol. Biol.* 337:513–519.
113. Marassi, F. M. 2001. A simple approach to membrane protein secondary structure and topology based on NMR spectroscopy. *Biophys. J.* 80:994–1003.
114. Marassi, F. M., and S. J. Opella. 2002. Using PISA pies to resolve ambiguities in angular constraints from PISEMA spectra of aligned proteins. *J. Biomol. NMR*. 23:239–242.
115. Kim, S., and T. A. Cross. 2002. Uniformity, ideality, and hydrogen bonds in transmembrane α -helices. *Biophys. J.* 83:2084–2095.